# Characteristics of gravity wave horizontal phase velocity spectra in the mesosphere over the Antarctic stations, Syowa and Davis

**Masaru Kogure[1], Takuji Nakamura[2,3], Damian J. Murphy[4], Michael J. Taylor[5], Yucheng Zhao[5], Pierre-Dominique Pautet[5], Masaki Tsutsumi[2,3], Yoshihiro Tomikawa[2,3], Mitsumu K. Ejiri[2,3], Takanori Nishiyama[2,3]**

[1] Department of Earth and Planetary Science, Kyushu University, Fukuoka, Japan.

[2] National Institute of Polar Research.

[3] Department of Polar Science, SOKENDAI (The Graduate University for Advanced Studies), Tachikawa, Japan.

[4] Australian Antarctic Division, Department of Agriculture, Water and the Environment, Kingston, Australia.

[5] Center for Atmospheric and Space Sciences/Physics Department, Utah State University, Logan, UT, USA.

Corresponding author: Masaru Kogure (kogure.masaru.695@m.kyushu-u.ac.jp)

**Key Points:**

- Mesospheric gravity-wave activity at two Antarctic stations was larger in winter than in spring and fall.
- The wave activity at Davis was larger in winter than Syowa but smaller in fall, which cannot be explained by the wind filtering effect.
- We demonstrated that gravity waves with ~100 $ms^{-1}$ eastward phase velocity at Davis were generated by primary gravity wave breaking.

## Abstract

Mesospheric gravity-wave (GW) phase velocity spectra and total powers at two Antarctic stations, Davis and Syowa, were derived using OH airglow image data from March to October in 2016. The total powers have similar seasonal variation, that is, maxima in winter at both stations. However, the power at Davis was one standard deviation larger in winter and three times smaller in September than at Syowa. The total power at Davis in winter was mainly attributed to GWs with high eastward ($\geq \sim 50\ \mathrm{ms}^{-1}$) phase velocity. On the other hand, the higher total power at Syowa in September was attributed to GWs with omnidirectional phase velocity. These differences between Syowa and Davis can not be explained by the wind filtering effect, and other factors are needed. To further explorer the origin of the difference in winter, we focused on an event on August 29, 2016, in which GWs with ~100 $\mathrm{ms}^{-1}$ southeastward phase velocity appeared at Davis. The raytracing method was applied, and its result indicated that those GWs with high southeastward phase velocity propagated from ~45 km altitude over the southern ocean ($\sim 43°\mathrm{E}, \sim 58°\mathrm{S}$) where GWs with high amplitude and southeastward propagating emitted from the tropospheric jet appeared. These jet GWs were probably saturated in 45-50 km altitudes. Therefore, the GWs with eastward phase velocity were probably secondary gravity waves. This result suggests that the higher power in the eastward high phase velocity domain at Davis was contributed to by secondary GWs.


## 1 Introduction

Gravity waves (GW) play an essential role in transporting momentum vertically and driving the circulation in the middle atmosphere (Fritts and Alexander, 2003). Current global

circulation models (GCMs) cannot resolve the full spectrum of GWs so that GW influences (GW drags) are parametrized in GCMs. Although the GW drag parameterization schemes improve the ability of GCMs to reproduce observations, they still poorly represent GW sources, spectra, local variability, and intermittency, which causes deviations between GCMs and the real atmosphere (Alexander et al., 2010). Inadequate knowledge of GWs is a key element of this limitation.

In order to understand GW sources and features, many studies have investigated GWs in the real atmosphere by using in-situ and remote sensing instruments. Airglow imaging is one remote sensing method that has high sensitivity to GWs with small horizontal wavelengths (~10s km) and short periods (several minutes). Such GWs deposit substantial momentum around the mesopause (Fritts and Vincent, 1987).

Matsuda et al. (2017) investigated the spatial variability of GW horizontal phase velocity around the edge of Antarctica by using observations from four OH airglow imagers during 1.5 months (April to May) at Syowa (69°S,40°E), Davis (69°S, 78°E), McMurdo (78°S, 167°E), and Halley (76°S, 26°E). These instruments which are operated by the Antarctic Gravity Wave Instrument Network (ANGWIN) showed that GW intermittency can be caused by the wind filtering effect, and the GW activity over the Antarctic was variable in latitude (the GW activities at Syowa and Davis were ~5 times larger than those at McMurdo and Halley). They also found that GW power spectral density (PSD) in eastward phase velocity less than $\sim 70\ \mathrm{ms}^{-1}$ was ~10 times larger at Davis than at Syowa. This large PSD at Davis was exceptional because the GWs with small eastward phase velocity could not reach the airglow layer from the troposphere at Davis, as well as Syowa. The paper mentioned that a possible source of those GWs may be secondary generation above the stratosphere, although it does not robustly demonstrate the

69 possible source. Also, it is uncertain that the large PSD in the eastward velocity is a common
70 feature at Davis because of the short (1.5 month) dataset.

71 The purpose of this study is to clarify differences in phase velocity spectra between Davis
72 and Syowa and to show statistically significant results by using a whole Austral winter season
73 (March to October) in 2016. Chapter 2 introduces OH airglow imagers at Syowa and Davis, and
74 data analysis. In Chapter 3, we show the differences of GW activities between Syowa and Davis,
75 and compare our results with Matsuda et al. (2017). We discuss the effects of wind filtering on
76 the GWs in Chapter 4 and investigate a source of GWs with eastward phase velocity at Davis.

77 **2. Observation and Data analysis.**

78 Two OH airglow imagers at Syowa (40°E, 69°S) and Davis (78°E, 69°S) are operated by
79 National Institute of Polar Research (NIPR) and the Utah State University, respectively. Both
80 imagers are equipped with indium gallium arsenide (InGaAs) detectors, which are sensitive to
81 wavelegths between 0.9-1.7$\mu m$, avoiding a large part of the auroral contamination (0.4-0.8 $\mu m$)
82 seen by CCD detectors (Matsuda et al., 2017). The detectors are incorporated with a Fujinon
83 FE185C086HA-1 C-mount fisheye lens to observe the whole sky. The specification of both

| Station | Latitude | Longitude | Operation Institution | Airglow[a] | Sampling Interval[b] | Exposure | Detector Size |
|---|---|---|---|---|---|---|---|
| Syowa | 69° S | 40° E | NIPR | OH (0.9-1.7$\mu$m) | 5 s | 2 s | 320×256 |
| Davis | 69° S | 78° E | USU | OH (0.9-1.7$\mu$m) | 10 s | 3 s | 320×256 |

[a] The OH layer altitude is assumed as 87 km.
[b] OH intensity images are averaged in 1 min.

84 imagers is summalized in Table 1.

85

Table 1. Summary of the two airglow imager specifications.

This study used the data without clouds, moon, and auroral contamination lasting for more than 1 hour from March to October 2016. Table 2 shows the distribution of the data windows, and this study analyzed 39 days at Syowa and 55 days at Davis.

| | | Mar. | Apr. | May | Jun. | Jul. | Aug. | Sep. | Oct. | Total |
|---|---|---|---|---|---|---|---|---|---|---|
| Syowa | Num. of night | 1 | 8 | 9 | 3 | 4 | 7 | 6 | 1 | 39 |
| | Total length (hour) | 1.0 | 17.9 | 35.7 | 11.4 | 14.8 | 23.5 | 12.2 | 1.3 | 117.5 |
| Davis | Num. of night | 6 | 6 | 7 | 2 | 8 | 11 | 10 | 5 | 55 |
| | Total length (hour) | 15.4 | 12.3 | 15.8 | 12.8 | 26.0 | 56.0 | 27.6 | 10.6 | 176.5 |

Table 2. The number of data windows used in this study. The criteria for choosing the data are (1) clear-sky, (2) without the moon, and (3) aurora-free images continued for > 1 hour.

To derive a GW phase velocity spectrum, an M-transform was applied to the OH airglow image data. Since the M-transform is described in Matsuda et al. (2014; 2017) and Perwitasari et al. (2018) in detail, only preprocesses are explained here. The raw image data were averaged to 1 min for compatibility between measurement cadences at Syowa and Davis and star and dark count removal was applied. To derive relative OH airglow intensity perturbations, the average night time intensity is subtracted from each 1 min image, the residual intensity ($I'$) was divided by the nightly mean ($I_0$), and then $I'/I_0$ was defined as the relative intensity perturbation. The $I'/I_0$ images were projected onto geographical coordinates, assuming a mean emission height of 87 km altitude (Baker and Stair, 1988). An OH emission height can vary between 79-88 km altitudes (Grygalashvyly et al., 2014; Nishiyama et al., 2021), but this causes less than 10 % phase speed error and the error can be neglected in this study. The M-transform was applied to

each $256 \times 256$ km$^2$ area image, centered on the zenith, with $1 \times 1$ km$^2$ pixel size . The spectral components with 5-100 km horizontal wavelengths, 8-60 min periods, and 0-150 ms$^{-1}$ phase speeds were extraced and regarded as representing GW intensities.

## 3. Comparison of GW activities between Syowa and Davis

Figure 1 shows total powers of the GWs, obtained using the PSD integrated in direction and phase speed from 0-150 ms$^{-1}$, over Davis and Syowa stations. The GW activity over both stations increased from March-April (fall) to May-August (winter) and decreased in September-October (spring). The total powers have similar seasonal variations, although the power at Davis was enhanced in late June to early July and late July to early August. On the other hand, the total power over Davis is in spring was three times smaller than that over Syowa.

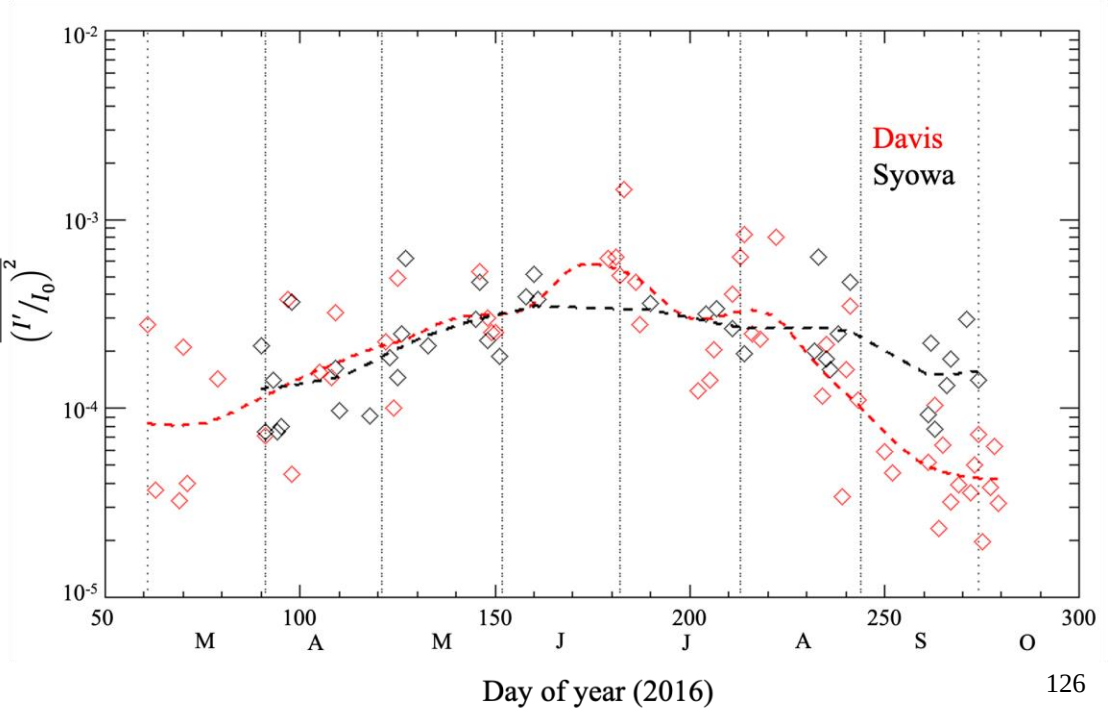

Figure 1. The red and black diamonds indicate total powers of GWs at Davis and Syowa, respectively. The red and black dashed lines indicate the smoothed total powers with logarithmic Gaussian weighting function ($\sigma = 15$ days, $width = 61$ days), respectively. It should be noted that the smoothed values have large uncertainty because of the sparse data.

Figure 2 follows Matsuda et al. (2017), but the total powers averaged in May-August and September over Davis and Syowa have been added. The powers over both stations were largest in May-August 2016, followed by April-May 2013 and September 2016. The total powers over Syowa and Davis in May-August, and over Syowa in September are larger than those over Halley and McMurdo in April-May, but the one over Davis in September is comparable.

The average power in May-August 2016 over Davis was larger than that over Syowa by $7 \times 10^{-5}$. This difference was larger than its one standard deviation ($5 \times 10^{-5}$), which was calculated from one standard deviation of the two average total powers over Syowa and Davis in May-August. However, the powers in April-May 2013 were similar between Davis and Syowa, and Matsuda et al. (2017) concluded that the powers over Syowa and Davis were not different significantly. This contradiction could be attributed to different sampling numbers. The numbers of sampling days in May-August 2016 (23 days at Syowa and 29 days at Davis) are about three times larger than those in April-May 2013 (9 days at Syowa and 8 days at Davis). The confidence intervals in May-August 2016 should be about $\sqrt{3}$ times smaller than those in April-May 2013 in Figure 2. Also, the total power in September over Davis was almost three times ($9 \times 10^{-5}$) smaller than that over Syowa, and this difference was larger than its standard deviation ($3 \times 10^{-5}$). Thus, the GW total powers have significant differences between Syowa and Davis.

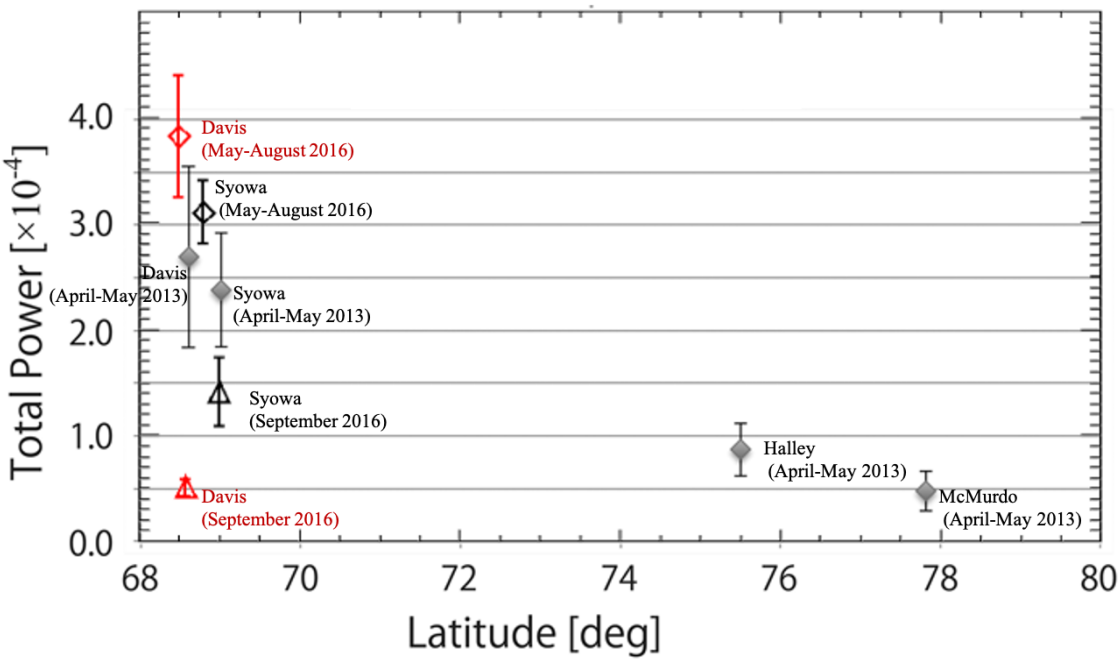


Figure 2. The red and black diamonds (triangles) indicate the mean total power in May to August (September) in Davis and Syowa, respectively. The gray diamonds indicate the mean total variance in April to May, 2013 [Matsuda et al., 2017]. These diamonds from right to left indicate the variances in Davis, Syowa, Halley, and McMurdo, respectively. The error bar indicates confidence interval of the average total power.

To further explore the different characteristics of the GWs between Davis and Syowa, the average phase velocity spectra for May-August and September are compared in Figure 3. The spectra for Syowa and Davis in Figures 3a, b, d, and e have the same directionality; that is, for phase speeds $\leq \sim 50\ \mathrm{ms}^{-1}$, the PSD between $180 - 360°$ clockwise from the north (westward) is larger than that in the same speed range between $0 - 180°$ clockwise (eastward). For phase speeds $\geq 80\ \mathrm{ms}^{-1}$, the result is reversed, and the PSD magnitude is for higher eastward waves. However, the spectral ratio ($PSD_{Davis}/PSD_{Syowa}$) in Figure 3c shows the PSD averaged in May-August around $45 - 180°$ clockwise from the north (northeast to southward), especially

167 $\geq \sim 50\ \mathrm{ms}^{-1}$, is larger over Davis than that over Syowa by one standard deviation in the PSD
168 difference. This result implies that the larger PSD for azimuth between $45 - 180°$ clockwise
169 from the north contributed to the higher winter mean total power at Davis. On the other hand, for
170 Septmber (Figure 3f), the PSD at Davis in September is smaller in almost the whole phase
171 velocity domain than that in Syowa by one standard deviation, implying the larger PSD in almost
172 the whole domain contributed to the larger total power at Syowa during the Spring. These
173 differences can be caused by the two possible mechanisms (1) wind filtering (2) wave
174 generation. In the following section, we will discuss these mechanisms.
175

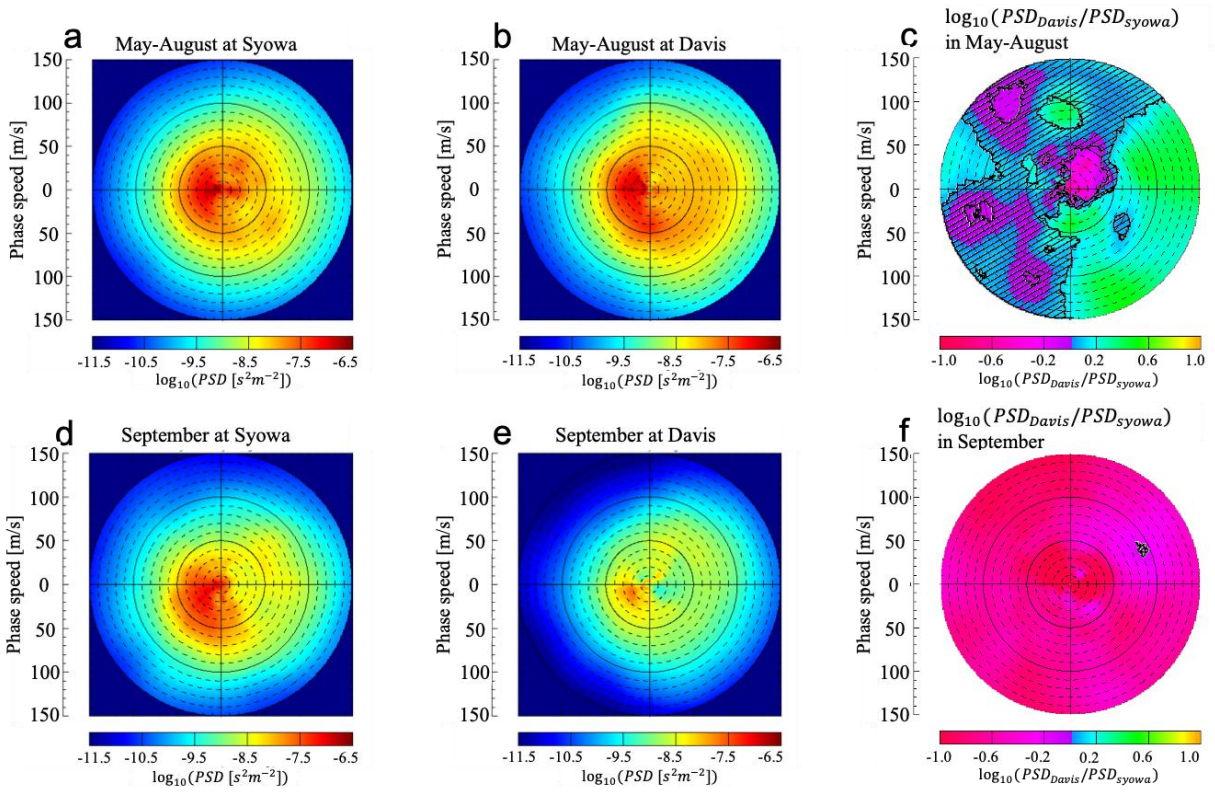

176

177 Figure 3. PSDs averaged in May-August and September at Syowa (a and b) and Davis (d and e),
178 respectively. Phase speed lines are separated by 10 m $s^{-1}$. Panels c and f show the ratio between

179 the PSDs at Syowa and Davis in May-August and September, respectively. The hatch areas
180 indicate that the ratio is within the confidence interval.
181

182 **4. Comparison between GW spectra and transmission diagrams**

183 To evaluate the wind filtering effect, the GW spectra were compared with transmission
184 diagrams. The transmission diagram shows the possibility of vertical propagation, for a GW on a
185 phase velocity spectrum, from the altitude of a wave emission up to the airglow layer altitude
186 (Tomikawa, 2015). The wave source and airglow altitudes are assumed to be 10 km and 87 km,
187 respectively. The diagrams were calculated from the winds and buoyancy frequencies averaged

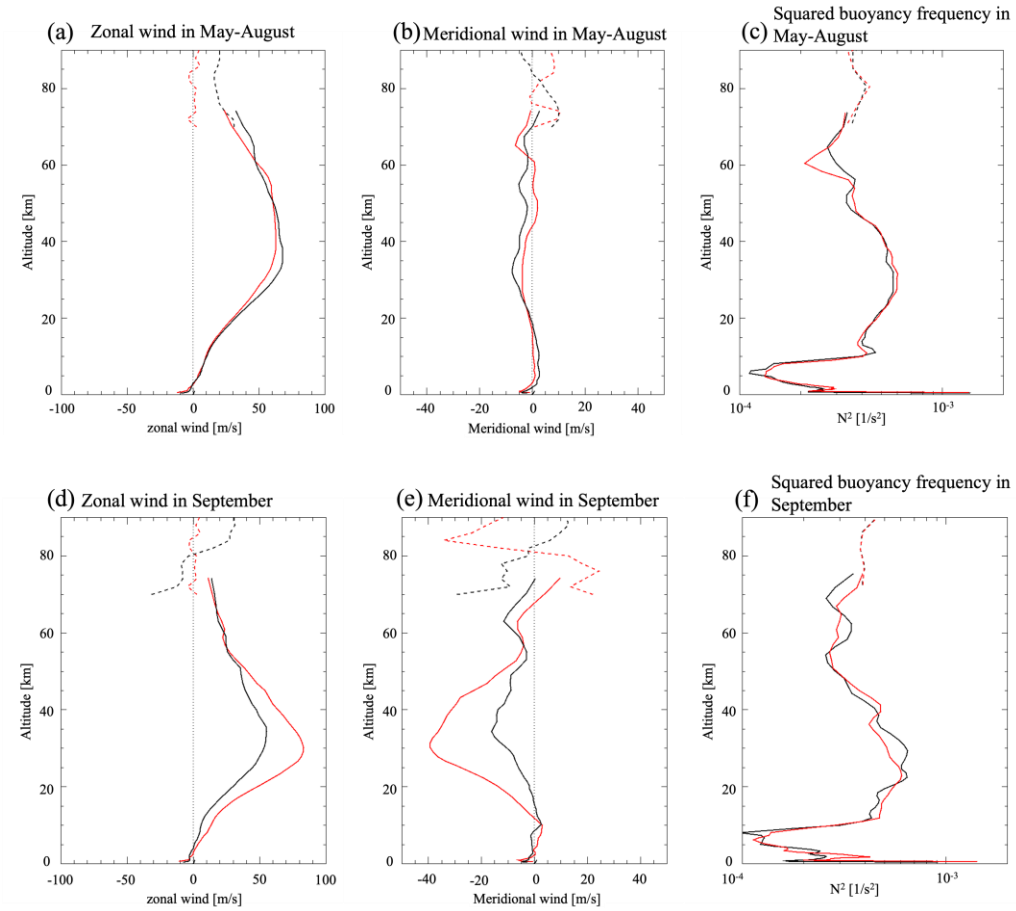

in May-August and September at each station (Figure 4).

Figure 4. (a) Mean zonal and (b) meridional wind, and (c) squared buoyancy frequency profiles in May to August in Syowa (black) and Davis (red), respectively. The solid lines indicate re-analysis, MERRA-2. The dashed lines indicate observations (MF radars and MLS/Aura). (d), (e), and (f) are the same as (a), (b), and (c), respectivity, but in September.

The winds and buoyancy frequencies below 70 km altitude are from The Modern-Era Retrospective Analysis for Research and Applications, Version 2, i.e., MERRA-2, (Gelaro et al., 2017), and those above the top of MERRA-2 were from observations, MF radars (Tsutsumi et al., 2001) and Aura Microwave Limb Sounder (MLS) (Waters et al., 2006). The values between 70 km and the top of MERRA-2 are averages between MERRA-2 and the observations calculated with a linear weighting function. Tomikawa (2015) pointed out that the propagation possibility significantly depends on a GW period so that the spectra in Figure 3 were divided into 6-period bands in accordance with Matsuda et al. (2017).

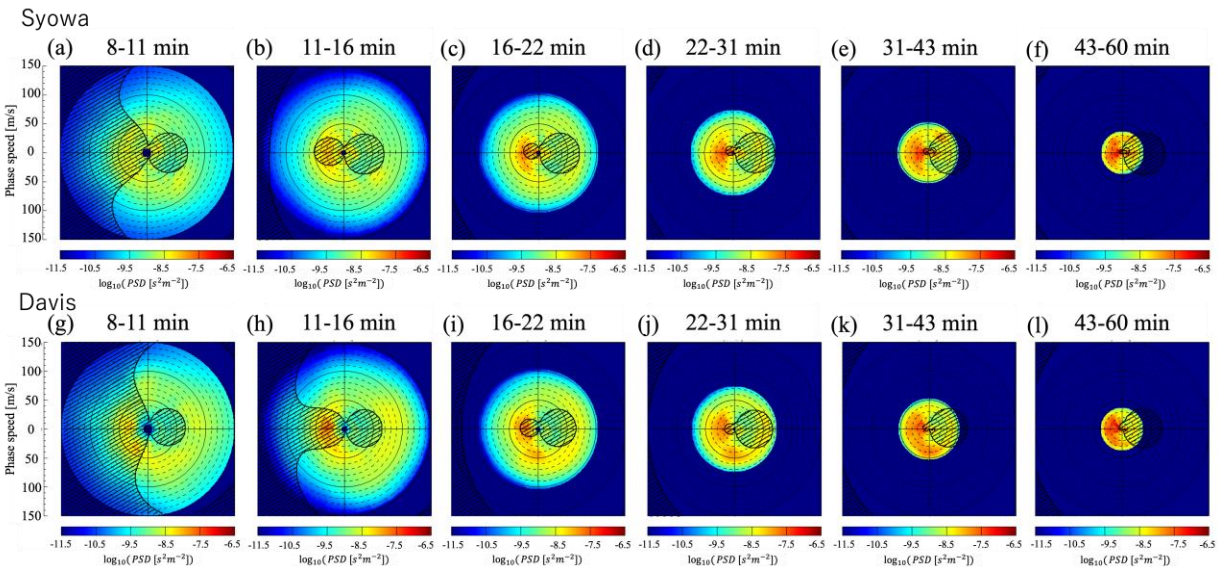

Figure 5. Comparison between the average spectra and transmission diagrams in May-August. The color plots indicate the mean spectra in Syowa and Davis in period ranges of 8-11, 11-16, 16-22, 22-31, 3-43, and 43-60 min, respectively. The shaded areas indicate prohibited areas for GWs to propagate into the mesopause region.

Figure 5 shows the comparison between the averaged spectra and transmission diagrams in May-August. The wind filtering effects at each period are almost the same at both stations; that is, the GWs with very short periods tended to be filtered in the westward phase velocity spectra, and the ones with the periods closer to an hour were filtered on the eastward phase velocity spectra less than ~70 $ms^{-1}$. This result shows that the wind filtering effect cannot explain the larger PSDs in eastward phase velocity in Davis. It should be noted that PSDs in the westward phase velocity spectra less than ~50 $ms^{-1}$ and 8-16 min periods were enhanced at both stations even though they should be filtered. This result suggests that those GWs were not generated below the assumed 10 km source altitude (i.e., the troposphere). Bossert et al. (2017) and Heale et al. (2017) showed that the saturation of large-scale (long period) GWs can generate small-scale secondary GWs in the mesosphere. These saturated waves should also have higher harmonic Fourier components in frequency and horizontal wavenumber domains. The PSDs in period range 31-60 min and westward phase velocity less than ~50 $ms^{-1}$ were also enhanced suggesting those GWs were saturated such that they might generate the small scale GWs and have higher harmonic Fourier components.

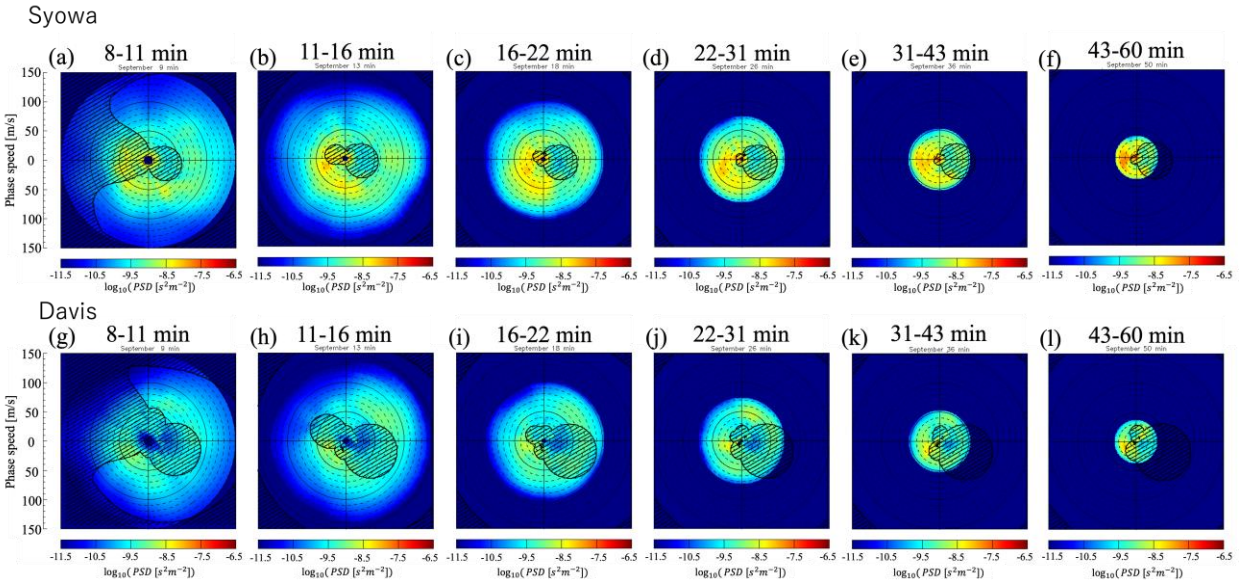


Figure 6 Comparison between the average spectra and transmission diagrams in September. The color plots indicate the mean spectra in Syowa and Davis in period ranges of 8-11, 11-16, 16-22, 22-31, 31-43, and 43-60 min, respectively. The shaded areas indicate prohibited areas for gravity waves.

Figure 6 is the same as Figure 5 but in September. The prohibited spectra in Davis were broadened into ~70-90 $ms^{-1}$ southeastward more widely than those in Syowa because of the stronger southward wind. This difference between the filtering effects can explain the larger PSD in ~70-90 $ms^{-1}$ southeastward phase velocity area in Syowa but cannot explain the PSD in the rest of the phase velocity area.

In summary, the filtering effect cannot explain the difference in May-August but can somewhat explain that in September. This result implies that other physical mechanisms should contribute more to the difference in the PSDs between Syowa and Davis. The possible mechanisms are (1) Horizontal propagation and (2) Source activity. The next section focuses on

an event for GWs with eastward phase velocity at Davis to further explorer the differences in May-August.

## 5. Event for GWs with high southeastward phase velocity at Davis on August 29, 2016

### 5.1. Origin altitudes of GWs on August 29, 2016.

Intense GWs with east to southward ($90 - 180°$ clockwise from the north) phase velocity higher than $\sim 50\ \mathrm{ms}^{-1}$ were observed at Davis on August 29, 2016, but not observed at Syowa. Figure7 shows the one-night mean spectra on August 29 at Syowa and Davis. Powers at Syowa and Davis were intense in southwestward phase velocity spectra with ~20-30 $ms^{-1}$, while the powers at Davis were larger in southeastward phase velocity spectra between 80-120 $ms^{-1}$ than those at Syowa. The features of the two PSDs are similar to those of the winter averages shown in Figure 3.

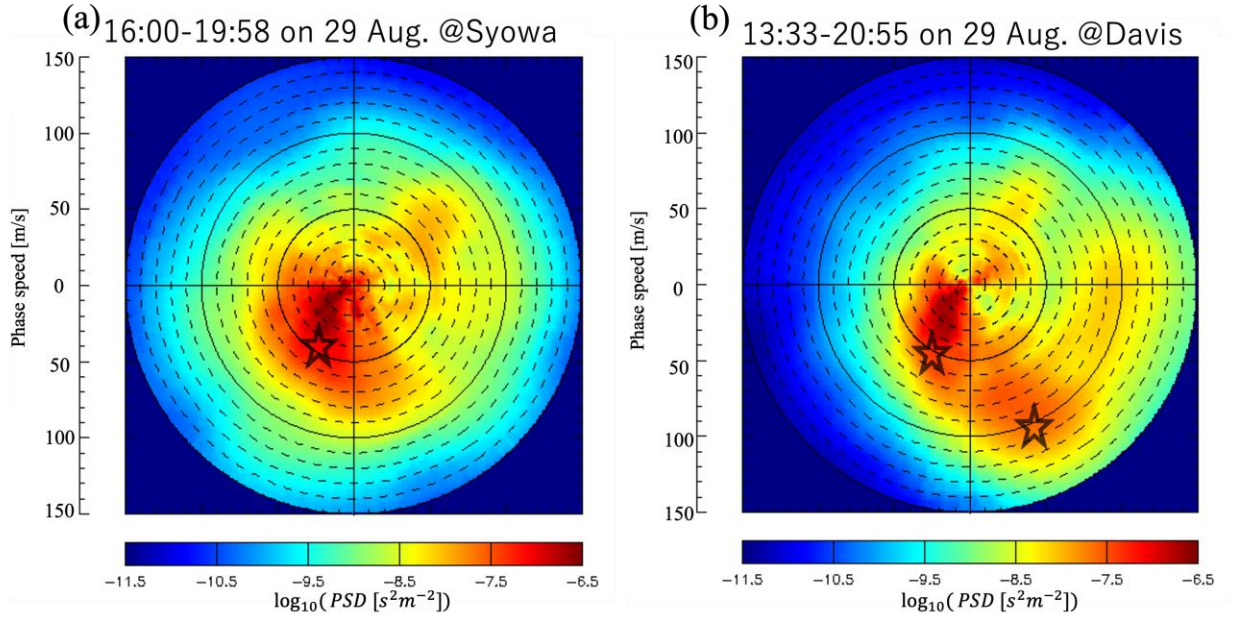

Figure 7. PSDs averaged on August 29, 2016, at Syowa (a) and Davis (b), respectively. The stars indicates initial phase velocities for raytracing method.

To explore where the GWs with ~100 $ms^{-1}$ southeastward phase velocity came from, we applied a backward raytracing method (Kogure et al., 2018; Kogure et al., 2020). The initial $\lambda_H$, $\tau$, $C_h$ are selected as values corresponding to the peaks of the power in ~30 $ms^{-1}$ southwest velocity spectra at Syowa and Davis, and ~100 $ms^{-1}$ southeast velocity spectra at Davis. Table 3 shows the initial parameters. The background wind and temperature below 70 km altitude were obtained from MERRA-2. Above the top of MERRA-2 (~74 km altitude), the background wind was measured by MF radars, and the temperature was measured from Aura MLS. Between 70 km and the top of MERRA-2, a linear weighting function was used to average between MERRA-2 and the observations. It should be noted that horizontal wind shear effects on wavelength were neglected above the top of MERRA-2.

| | No. | $\lambda_H$[km] | $\tau$[min] | $C_h$[m/s] | Direction [degree] | Terminal height [km] |
|---|---|---|---|---|---|---|
| Syowa | S1 | 84 | 30 | 46 | 209 | 0.1 |
| Davis | D1 | 28 | 9 | 52 | 207 | 9.2 |
| | D2 | 88 | 14 | 103 | 156 | 44.5 |

Table 3. Initial raytracing parameters for hydroxyl layer gravity waves

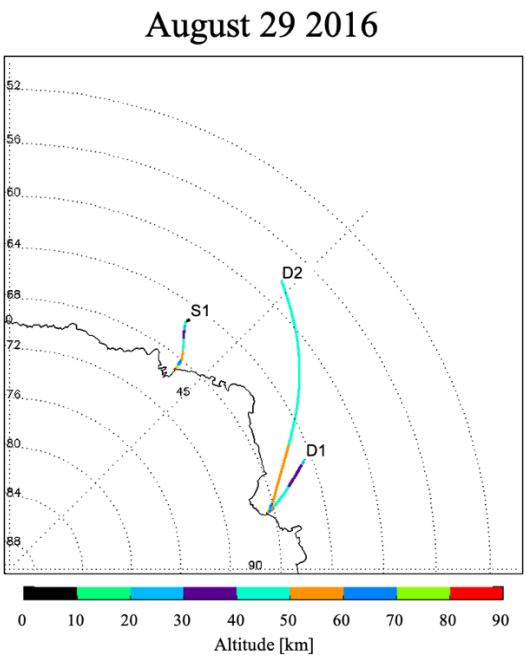


Figure 8. The backward raytracing method results for the GWs described in Table 3.

The backward raytracing results in Figure 8 show the three GWs propagated from the southern ocean. While the S1 and D1 (southwestward phase velocities) can propagate from 0.1 and 9.2 km altitudes, respectively, the D2 (southeastward phase velocity) back trace terminated at 44.5 km altitude because of a critical level. This result indicates that D2 could not have originated from below that level and must have been generated in the upper stratosphere. Rourke et al. (2017) observed such gravity waves with eastward phase velocity over Davis. This work also showed that those waves originated from the upper stratosphere by using the raytracing method, although it used empirical model background fields and did not determine the wave sources.

### 5.2. The possible GW sources in the stratosphere.

The possible sources for the D2 GW (southeastward phase velocity) in the stratosphere are (1) spontaneous adjustment (Plougonven and Zhang, 2014), and (2) secondary wave

generation (Vadas & Becker, 2019; Kogure et al., 2020). The residual of the nonlinear balance equation ($\Delta NBE$) from Plougonven and Zhang (2014) using MERRA-2 fields was not enhanced around the termination point so that the spontaneous adjustment mechanism can be ruled out (not shown). On the other hand, the Atmospheric Infrared Sounder (AIRS) aboard NASA's Aqua satellite captured two intense GWs near the termination point (~42E, ~58S) at ~9:40 UT in the 15 $\mu m$ high channel, which, in the polar region, is most sensitive to GW temperature peturbations at ~38 km altitude (Figure 9 (a)). (Channel response data can be acquired from https://datapub.fz-juelich.de/slcs/airs/gravity_waves/ (Hoffman et al., 2013; 2017)). The 15 $\mu m$ low channel of AIRS, which is most sensitive to GW temperature peturbation at ~23 km altitude, also captured two intense GWs in a similar area (not shown). These observed GWs appeared in the leeward of the geopotential height ridge at 200 hPa suggesting the waves were emitted from the tropospheric jet through spontaneous adjustment (Plougonven and Zhang, 2014).

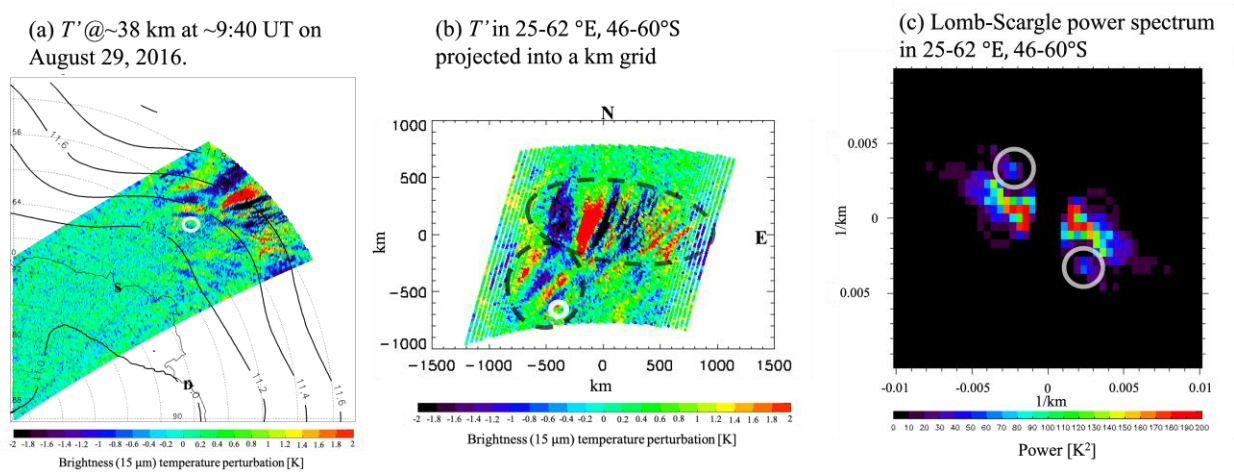


Figure 9. (a) Temperature perturbations observed by AIRS at ~38 km altitude at ~9:40 UT on August 29, 2016. The contour shows geopotential heights at 200 hPa. The white circlecorresponds to the termination of the D2 wave. (b) The Temperature perturbations in 25-62°E, 46-60°S projected onto a km grid. The white circle indicates the terminal point of the D2

GW (with southeastward phase velocity observed over Davis). (c) The Lomb-Scargle power spectrum of the temperature perturbations in 25-62°E, 46-60°S .

The AIRS data were projected onto a km grid in Figure 9 (b). There are two GWs apparent, with ~500 km and ~200 km horizontal wavelengths. The GW with ~200 km horizontal wavelength is situated near the termination of the D2 ray. Such intense GWs observed by AIRS could be saturated and have generated secondary gravity waves in the upper stratosphere and the mesosphere due to shear and/or convective instabilities (Bossert et al., 2015; Heale et al., 2020; Kogure et al., 2020). To investigate the saturation of the GWs, we calculate the local Richardson number, *Ri*, along a forward ray path. This analysis is similar to Kogure et al. (2020) with the exception that this study assumes wave action conservation; previously it was assumed that the growth rate of wave amplitude was the square root of density. To determine an initial horizontal vector for the forward raytracing, the AIRS data in Figure 9(b) is subject to 2D Lomb-Scargle spectral analysis. Figure 9(c) shows the Lomb-Scargle power spectrum where two local maxima in the spectrum can be seen. The local power maxima with 241 km horizontal wavelength and a direction of 146° or 214° clockwise from north correspond to the GW with ~200 km horizontal wavelength in Figure 9(b). The 2D Lomb-Scargle analysis has 180° ambiguity, but 146° is adopted here because the phase speed of a GW emitted from a jet is expected to match the phase speed of a baroclinic wave, i.e., eastward (Plougonven and Snyder, 2007). Murphy et al.(2014) also frequently observed GWs in radiosonde data with eastward phase velocity, which were potentially emitted from the jet, in the lower stratosphere over Davis but rarely observed westward GWs.

The measured amplitude of the GW with a 241 km horizontal wavelength is ~2 K in Figure 9(a) and (b), but this drastically underestimates the true amplitude (Hoffman et al., 2013; 2017). A response rate of the AIRS high 15 μm kernel is estimated using the AIRS vertical kernel investigation (https://datapub.fz-juelich.de/slcs/airs/gravity_waves/data/kernel.pdf), and the amplitude of the raytraced GW was compensated accordingly. However, the response rate and peak of the AIRS kernel varies in location and season, which causes ambiguities of the amplitude and the altitude used to launch the ray. Due to these ambiguities, the response rate and the initial altitude are varied by 3% and 2 km, respectively. The AIRS instrument cannot observe wave period, but the GWs emitted from jets tend to have a long ground-based period. Here, the period was trialled at 3, 5, and 10 hours.

The altitudes at which $Ri < 0.25$ for the trial GWs, which corresponding to potential start of saturation, are given in Table 4. Figure 10 shows the forward raytracing result for the GW with 3 hour ground-based period from 38 km altitude. This GW began to be saturated at almost the same point (diamond mark) as the D2 termination (white circle) on the horizontal surface although the saturation altitude is ~3 km higher than the D2 termination altitude. Precise agreement between the D2 termination height and the saturation height is not needed because the D2 wave could have been launched above the backward ray tracing termination height (but not below). GWs launched from similar horizontal positions but with the other parameters also propagated in the same direction (i.e., Davis ward) but the propagation paths and saturation altitudes varied. The saturation altitude of the GWs with the 3 hour ground-based period was closer to altitudes of the D2 path than those for 5 and 10 hours. It should be noted that Murphy et al. (2014) occasionally observed GWs with eastward and 22 $ms^{-1}$ phase speed (from 241 km/3 hours) in the lower stratosphere over Davis that are consistent with this wave. Making the

assumption that the southoeast propagating GW in the AIRS data had ~3 hour period, it can be asserted that the wave saturated at ~45-50 km. Since characteristic scales and directions of a secondary GW depend on a half scale and direction of a local body force, respectively (Vadas et al., 2003; Heale et al., 2020), the jet GW could cause a local body force with southeastward direction and ~44 km horizontal scale (a half of D2 GW horizontal wavelength). This local body force could create the GWs with ~100 $ms^{-1}$ southeastward phase velocity. Otherwise, the GWs over Davis could be generated through nonliner fluid interactions (Andreassen et al., 1998; Bossert et al., 2015; Fritts et al., 1994, 1998; Heale 2017).Thus, the GWs with ~100 $ms^{-1}$ southeastward phase velocity over Davis were very likely secondary GWs generated by the intense GW activity above the southern ocean.

| Period (hour) | Initial altitude | Response rate of AIRS kernel (%) | Initial amplitude (K) | Bottom height Ri < 0.25 (km) | Initial vertical wavelength (km) |
|---|---|---|---|---|---|
| 3 | 36 | 10 (7, 13) | 20 (29, 15) | 46 (39, 49) | 16 |
| 3 | 38 | 10 (7, 13) | 20 (29, 15) | 48 (41, 59) | 16 |
| 3 | 40 | 10 (7, 13) | 20 (29, 15) | 49 (46, 51) | 16 |
| 5 | 36 | 14 (11, 17) | 14 (18, 12) | 50 (48, 51) | 18 |
| 5 | 38 | 16 (13, 19) | 13 (15, 11) | 51 (51, 53) | 19 |
| 5 | 40 | 16 (13, 19) | 13 (15, 11) | 53 (52, 56) | 19 |
| 10 | 36 | 17 (14, 20) | 12 (14,10) | 52 (51,53) | 20 |
| 10 | 38 | 19 (16, 22) | 11 (13, 9) | 55 (53, 57) | 21 |
| 10 | 40 | 19 (16, 22) | 11 (13, 9) | 57 (55, 59) | 21 |

Table 4. Parameters for GW with a 241 km horizontal wavelength in the AIRS data on August 29, 2016. The initial amplitudes are 2 K (which is observed by AIRS) × the inverse of the response rate of the AIRS vertical kernel based on Figure 1 in Hoffmann et al. (2017). The values in parentheses are corresponding to the response rate −3 % and +3 %, respectively.

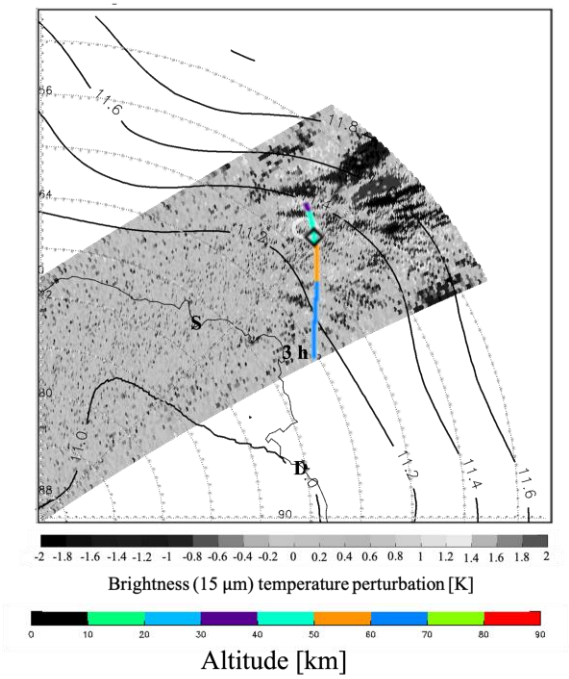


Figure 10. Raytracing result for the GWs with southeast horizontal wavevector superimposed in Figure 9(a). Its ground-based period, initial height, and initial temperature amplitude were assumed as 3 hour, 38 km, and 20 K, respectively. The diamamond indicates a bottom altitude with Ri < 0.25.

## 6. Conclusion

We compared the GW total powers and phase velocity spectra in the OH layer at two Antarctic stations, Davis and Syowa, from March to October 2016. The total powers showed maxima in winter and have similar seasonal variation at both stations. The powers at Davis were one standard deviation higher in winter and three times smaller in September than those at Syowa, respectively, although Matsuda et al. (2017) concluded that the powers at both stations were not significantly different at those times in 2013. This contradiction could be attributed to different sampling numbers, as our sampling numbers are about three times larger than those in Matsuda et al. (2017). The larger total power at Davis in winter was attributed to GWs with high

eastward ($\geq \sim 50\ \mathrm{ms}^{-1}$) phase velocity. On the other hand, the larger total power at Syowa in September was attributed to GWs with omnidirectional phase velocity. To evaluate background meteological field impacts on the GWs at both stations, we compared the spectra and transmission diagrams and then concluded that filtering effects cannot explain the differences in May-August but somewhat explain them in September. To further explore the causes of the differences between Syowa and Davis in May-August, we focused on a GW event with eastward phase velocity at Davis. The raytracing method indicated that those GWs propagated from ~45 km altitude over the southern ocean (~43°E, ~58°S), where GWs emitted from the tropospheric jet were apparent. These tropospheric jet GWs were probably saturated in 45-50 km altitudes and caused a ~44 km horizontal scale (a half of the GW horizontal wavelength over Davis ) local southeastward body force. Otherwise, the GWs over Davis could be generated through nonliner fluid interactions. Therefore, the GWs with eastward phase velocity observed in the mesosphere were secondary gravity waves. This result suggests that the larger PSD in eastward phase velocity at Davis in May-August was attributed to secondary GWs, that secondary GWs may contribute to GW phase velocity spectra in the mesosphere and that they cause non-negligible GW longitudinal variations. The larger total power in Syowa in September might be attributed to differences in a GW source activity or/and generation mechanisms between Syowa and Davis, but futuher study is needed to verify this.

## Acknowledgments, Samples, and Data

This work is supported by the JSPS grant JRPs-LEAD with DFG program, JSPS KAKENHI Grant Number 19K23465, JSPS Overseas Challenge Program for Young Researchers (No. 201780038), and the Scientific Committee on Antarctic Research (SCAR) fellowship award 2019. Support for the operation of the Davis MF radar and its analysis was provided through

AAS project number 4025, 4056 and 4445. The USU all-sky OH imager operated at Davis Station and its data analysis are supported by NSF #1143587 and NSF # 1443730. MERRA-2 data were obtained at http://disc.sci.gsfc.nasa.gov. MLS_Aura data were obtained at https://mls.jpl.nasa.gov/index-eos-mls.php. The AIRS/Aqua gravity wave data sets (Hoffmann et al., 2017) are provided by Forschungszentrum Jülich (https://datapub.fz-juelich.de/slcs/airs/gravity_waves/data). The daily average phase velocity spectra data at both stations can be obtained at http://id.nii.ac.jp/1291/00016369/. The MF radar data averaged in winter and September can be obtained at http://id.nii.ac.jp/1291/00016368/ . The M-transform program can be obtained at http://polaris.nipr.ac.jp/~airglow/M-transform/.

406

407 **References**

408 Alexander, M.J., Geller, M., McLandress, C., Polavarapu, S., Preusse, P., Sassi, F., Sato, K., et
409 al. (2010). Recent developments in gravity-wave effects in climate models and the global
410 distribution of gravity-wave momentum flux from observations and models. *Quarterly*
411 *Journal of the Royal Meteorological Society.*, 136: 1103-1124, doi:10.1002/qj.637.

412 Alexander, S. P., A. R. Klekociuk, & T. Tsuda (2009), Gravity wave and orographic wave
413 activity observed around the Antarctic and Arctic stratospheric vortices by the COSMIC
414 GPS-RO satellite constellation, *Journal of Geophysical Research.*, 114, D17103,
415 doi:10.1029/2009JD011851.

416 Andreassen, Ø., Hvidsten, P., Fritts, D., & Arendt, S. (1998). Vorticity dynamics in a breaking
417 internal gravity wave. Part 1. Initial instability evolution. *Journal of Fluid Mechanics*, 367,
418 27–46. doi: 10.1017/S0022112098001645

419 Baker, D. J., & Stair Jr, A. T. (1988). Rocket measurements of the altitude distributions of the
420 hydroxyl airglow. *Physica scripta*, 37(4), 611, doi: 10.1088/0031-8949/37/4/021

421 Bossert, K., Fritts, D. C., Pautet, P.-D., Williams, B. P., Taylor, M. J., Kaifler, B., Dörnbrack, A.,
422 et al. (2015), Momentum flux estimates accompanying multiscale gravity waves over
423 Mount Cook, New Zealand, on 13 July 2014 during the DEEPWAVE campaign, *Journal of*
424 *Geophysical Research: Atmospheres*, 120, 9323– 9337, doi:10.1002/2015JD023197.

425 Bossert, K., Kruse, C. G., Heale, C. J., Fritts, D. C., Williams, B. P., Snively, J. B., Pautet, P.-D.,
426 and Taylor, M. J. (2017), Secondary gravity wave generation over New Zealand during the

427 DEEPWAVE campaign, J. Geophys. Res. Atmos., 122, 7834– 7850,
428 doi:10.1002/2016JD026079.

429 Bossert, K., Fritts, D. C., Pautet, P.-D., Williams, B. P., Taylor, M. J., Kaifler, B., et al. (2015).
430 Momentum flux estimates accompanying multiscale gravity waves over mount cook, New
431 Zealand, on 13 July 2014 during the DEEPWAVE campaign. *Journal of Geophysical*
432 *Research: Atmospheres*, 120, 9323–9337. doi: 10.1002/2015JD023197.

433 Fritts, D. C., & Alexander, M. J. (2003), Gravity wave dynamics and effects in the middle
434 atmosphere, *Reviews of Geophysics*, 41, 1003, doi:10.1029/2001RG000106, 1.

435 Fritts, D. C., Arendt, S., & Anderassen, Ø. (1998). Vorticity dynamics in a breaking internal
436 gravity wave. Part 2. Vortex interactions and transition to turbulence. *Journal of Fluid*
437 *Mechanics*, 367, 47–65. doi: 10.1017/S0022112098001633

438 Fritts, D. C., Isler, J. R., & Andreassen, Ø. (1994). Gravity wave breaking in two and three
439 dimensions: 2. Three-dimensional evolution and instability structure. *Journal of*
440 *Geophysical Research*, 99(D4), 8109–8123. doi: 10.1029/93JD03436

441 Fritts, D. C., & Vincent, R. A. (1987). Mesospheric Momentum Flux Studies at Adelaide,
442 Australia: Observations and a Gravity Wave–Tidal Interaction Model, *Journal of*
443 *Atmospheric Sciences*, 44(3), 605-619, doi:10.1175/1520-
444 0469(1987)044<0605:MMFSAA>2.0.CO;2

445 Gelaro, R., McCarty, W., Suárez, M. J., Todling, R., Molod, A., Takacs, L., Randles, C. A., et al.
446 (2017). The Modern-Era Retrospective Analysis for Research and Applications, Version 2
447 (MERRA-2), *Journal of Climate*, 30(14), 5419-5454, doi: 10.1175/JCLI-D-16-0758.1.

Grygalashvyly, M., Sonnemann, G. R., Lübken, F.-J., Hartogh, P., and Berger, U. (2014), Hydroxyl layer: Mean state and trends at midlatitudes, *J. Geophys. Res. Atmos.*, 119, 12,391– 12,419, doi:10.1002/2014JD022094.

Heale, C. J., Bossert, K., Snively, J. B., Fritts, D. C., Pautet, P.-D., and Taylor, M. J. (2017), Numerical modeling of a multiscale gravity wave event and its airglow signatures over Mount Cook, New Zealand, during the DEEPWAVE campaign, *J. Geophys. Res. Atmos.*, 122, 846– 860, doi:10.1002/2016JD025700.

Heale, C. J., Bossert, K., Vadas, S. L., Hoffmann, L., Dörnbrack, A., Stober, G., B. Snively, et al. (2020). Secondary gravity waves generated by breaking mountain waves over Europe. *Journal of Geophysical Research: Atmospheres*, 125, e2019JD031662, doi:10.1029/2019JD031662

Hoffmann, L., X. Xue, & M. J. Alexander. (2013). A global view of stratospheric gravity wave hotspots located with Atmospheric Infrared Sounder observations, *Journal of Geophysical Research: Atmospheres*, 118, 416-434, doi:10.1029/2012JD018658.

Hoffmann, L., Spang, R., Orr, A., Alexander, M. J., Holt, L. A., & Stein, O. (2017), A decadal satellite record of gravity wave activity in the lower stratosphere to study polar stratospheric cloud formation, *Atmospheric Chemistry and Physics*, 17, 2901-2920, doi:10.5194/acp-17-2901-2017.

Kaifler, B., F. J. Lübken, J. Höffner, R. J. Morris, and T. P. Viehl (2015), Lidar observations of gravity wave activity in the middle atmosphere over Davis (69°S, 78°E), *Journal of Geophysical Research: Atmospheres*, 120, 4506– 4521, doi:10.1002/2014JD022879.

Kogure, M., Nakamura, T., Ejiri, M. K., Nishiyama, T., Tomikawa, Y., Tsutsumi, M., Suzuki, et al. (2017). Rayleigh/Raman lidar observations of gravity wave activity from 15 to 70 km altitude over Syowa (69°S, 40°E), the Antarctic, *Journal of Geophysical Research: Atmospheres*, 122, 7869– 7880, doi:10.1002/2016JD026360.

Kogure, M., Nakamura, T., Ejiri, M. K., Nishiyama, T., Tomikawa, Y., & Tsutsumi, M. (2018). Effects of horizontal wind structure on a gravity wave event in the middle atmosphere over Syowa (69°S, 40°E), the Antarctic. *Geophysical Research Letters*, 45, 5151– 5157. doi:10.1029/2018GL078264.

Kogure, M., Yue, J., Nakamura, T., Hoffmann, L., Vadas, S. L., Tomikawa, Y., et al. (2020). First direct observational evidence for secondary gravity waves generated by mountain waves over the Andes. *Geophysical Research Letters*, 47, e2020GL088845. Doi:10.1029/2020GL088845

Matsuda, T. S., Nakamura, T., Ejiri, M. K., Tsutsumi, M., and Shiokawa, K. (2014), New statistical analysis of the horizontal phase velocity distribution of gravity waves observed by airglow imaging, *Journal of Geophysical Research: Atmospheres.*, 119, 9707– 9718, doi:10.1002/2014JD021543.

Matsuda, T. S., Nakamura, T., Ejiri, M. K., Tsutsumi, M., Tomikawa, Y., Taylor, M. J., Zhao, Y., Pautet, P.-D., Murphy, D. J., and Moffat-Griffin, T. (2017), Characteristics of mesospheric gravity waves over Antarctica observed by Antarctic Gravity Wave Instrument Network imagers using 3-D spectral analyses, *Journal of Geophysical Research: Atmospheres*, 122, 8969– 8981, doi:10.1002/2016JD026217.

Murphy, D. J., Alexander, S. P., Klekociuk, A. R., Love, P. T., and Vincent, R. A. (2014), Radiosonde observations of gravity waves in the lower stratosphere over Davis, Antarctica, *J. Geophys. Res. Atmos.*, 119, 11,973– 11,996, doi:10.1002/2014JD022448.

Nappo, C. J. (2013). An introduction to atmospheric gravity waves. *Academic press*.

Nishiyama, T., Taguchi, M., Suzuki, H., Dalin, P., Ogawa, Y., Brändström, T., et al. (2021), Temporal evolutions of $N_2^+$ Meinel (1,2) band near 1.5.μm associated with aurora breakup and their effects on mesopause temperature estimations from OH Meinel (3,1) band. *Earth Planets Space* **73,** 30, doi:10.1186/s40623-021-01360-0

Plougonven, R., & Snyder, C. (2007). Inertia–Gravity Waves Spontaneously Generated by Jets and Fronts. Part I: Different Baroclinic Life Cycles, *Journal of the Atmospheric Sciences*, 64(7), 2502-2520. doi: 10.1175/JAS3953.1

Plougonven, R., and Zhang, F. (2014), Internal gravity waves from atmospheric jets and fronts, *Reviews of Geophysics*, 52, 33– 76, doi:10.1002/2012RG000419.

Rourke, S., Mulligan, F. J., French, W. J. R., & Murphy, D. J. (2017). A climatological study of short-period gravity waves and ripples at Davis Station, Antarctica (68°S, 78°E), during the (austral winter February–October) period 1999–2013. *Journal of Geophysical Research: Atmospheres*, 122. doi:10.1002/2017JD026998

Septi Perwitasari, Takuji Nakamura, Masaru Kogure, Yoshihiro Tomikawa, Mitsumu K. Ejiri, Kazuo Shiokawa (2018), Comparison of gravity wave propagation directions observed by mesospheric airglow imaging at three different latitudes using the M-transform, *Annales Geophysicae*, 36, 6, (1597-1605), doi: 10.5194/angeo-36-1597-2018.

Tomikawa, Y. (2015), Gravity wave transmission diagram, *Annales Geophysicae*, 33, 1479–1484, doi:10.5194/angeo-33-1479-2015.

Tsutsumi, M., Aso, T. and Ejiri, M.. (2001), Initial results of Syowa MF radar observations in Antarctica, *Adv. Polar Upper Atmosphere research*, 15, 103-116, doi:10.15094/00006333.

Vadas, S. L., and Becker, E. (2019). Numerical modeling of the generation of tertiary gravity waves in the mesosphere and thermosphere during strong mountain wave events over the Southern Andes. *Journal of Geophysical Research: Space Physics*, 124, 7687– 7718.

Vadas, S. L., Fritts, D. C., & Alexander, M. J. (2003). Mechanism for the generation of secondary waves in wave breaking regions. *Journal of the Atmospheric Sciences*, 60(1), 194–214. doi: 10.1175/1520-0469(2003)060<0194:MFTGOS>2.0.CO;2

Waters, J. W., Froidevaux, L., Harwood, R. S., Jarnot, R. F., Pickett, H. M., Read, W. G., Siegel, P. H., et al. (2006). The Earth observing system microwave limb sounder (EOS MLS) on the aura Satellite, *in IEEE Transactions on Geoscience and Remote Sensing*, 44, 5, 1075-1092, doi: 10.1109/TGRS.2006.873771.